

Dynamic multiple-target tracing to probe spatiotemporal cartography of cell membranes

Arnauld Sergé, Nicolas Bertaux, Hervé Rigneault & Didier Marguet

Supplementary figures and text:

Supplementary Figure 1 | Specificity of Qdot fluorescence

Supplementary Figure 2 | Illustration of MTT computation

Supplementary Figure 3 | Confinement level calibration

Supplementary Figure 4 | Evaluation of confinement models

Supplementary Figure 5 | MTT at increased acquisition rate

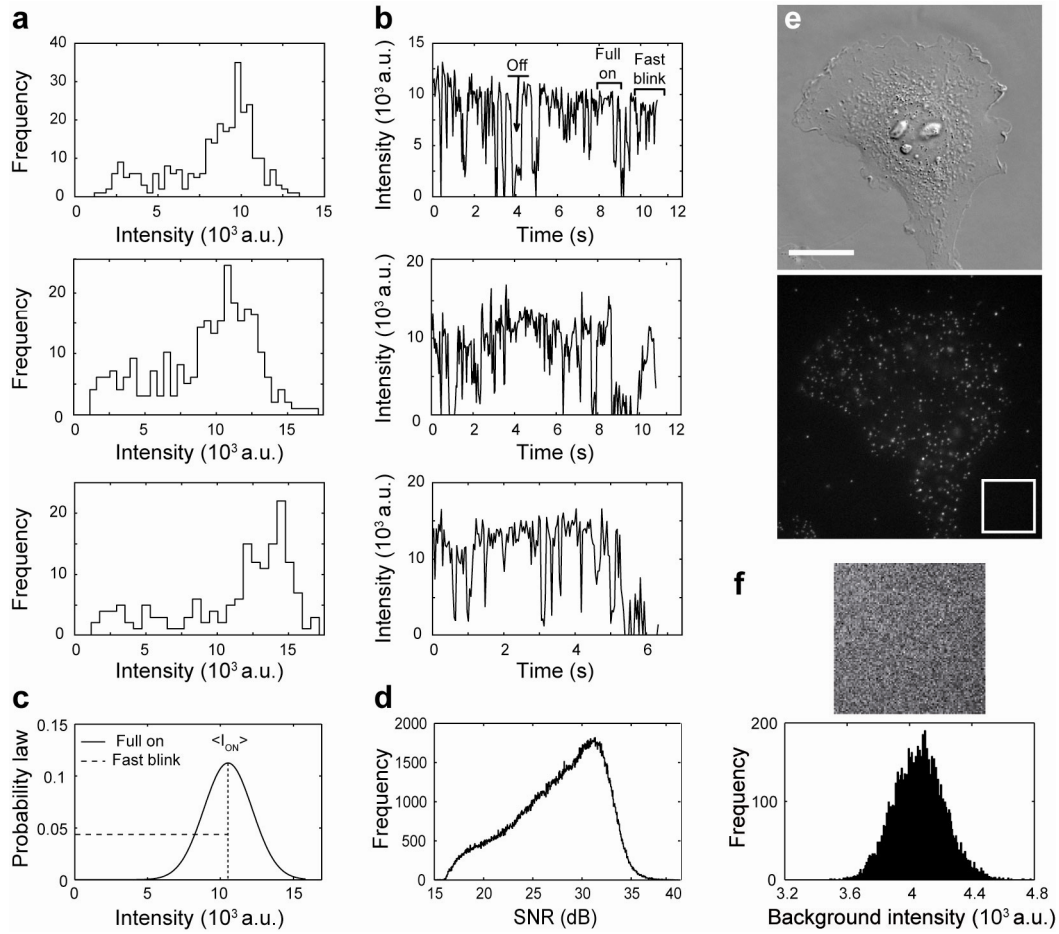
Supplementary Table 1 | Glossary of fluorescence peak, trajectory, and free and confined event descriptors.

Supplementary Methods | Monte Carlo simulations, cell culture and Qdot staining, equipment and settings.

Supplementary Note | MTT algorithm principle, tutorial of signal detection concepts and mathematical appendices.

Note: Supplementary Videos 1–3 are available on the Nature Methods website.

Supplementary Figure 1



Specificity of Qdot fluorescence (a) Typical histograms of intensities, from single Qdot traces, depicting a mix of high and intermediate values, related to full on and fast blinking periods, respectively. (b) Corresponding graphs of intensity fluctuations with time, depicting full on, fast (compared to acquisition time) blinking and off periods. (c) Associated theoretical probability law, updated when a particle is estimated as being on (see **Mathematical Appendix 2**). (d) The SNR distribution ($n=5$ cells) displays a major peak at ~ 30 dB (corresponding to a peak amplitude ~ 15 times above noise), corresponding to full on measures, and intermediate values down to ~ 15 - 20 dB (peak amplitude ~ 5 times above noise), mostly due to fast blink. (e) DIC image of a COS-7 cell (top) at 100 ms acquisition time and without amplification. Scale bar, 10 μ m. Corresponding epifluorescence image (bottom) from a stack acquired at 36 ms/frame. (f) Gaussian modeling of the background noise. Top: zoom of the background evaluated from experimental data (area framed in e). Bottom: histogram of the gray levels present in the zoom. The mean offset m and the standard deviation of the noise σ are similarly estimated locally, within the sliding window used for detection.

Supplementary Figure 2

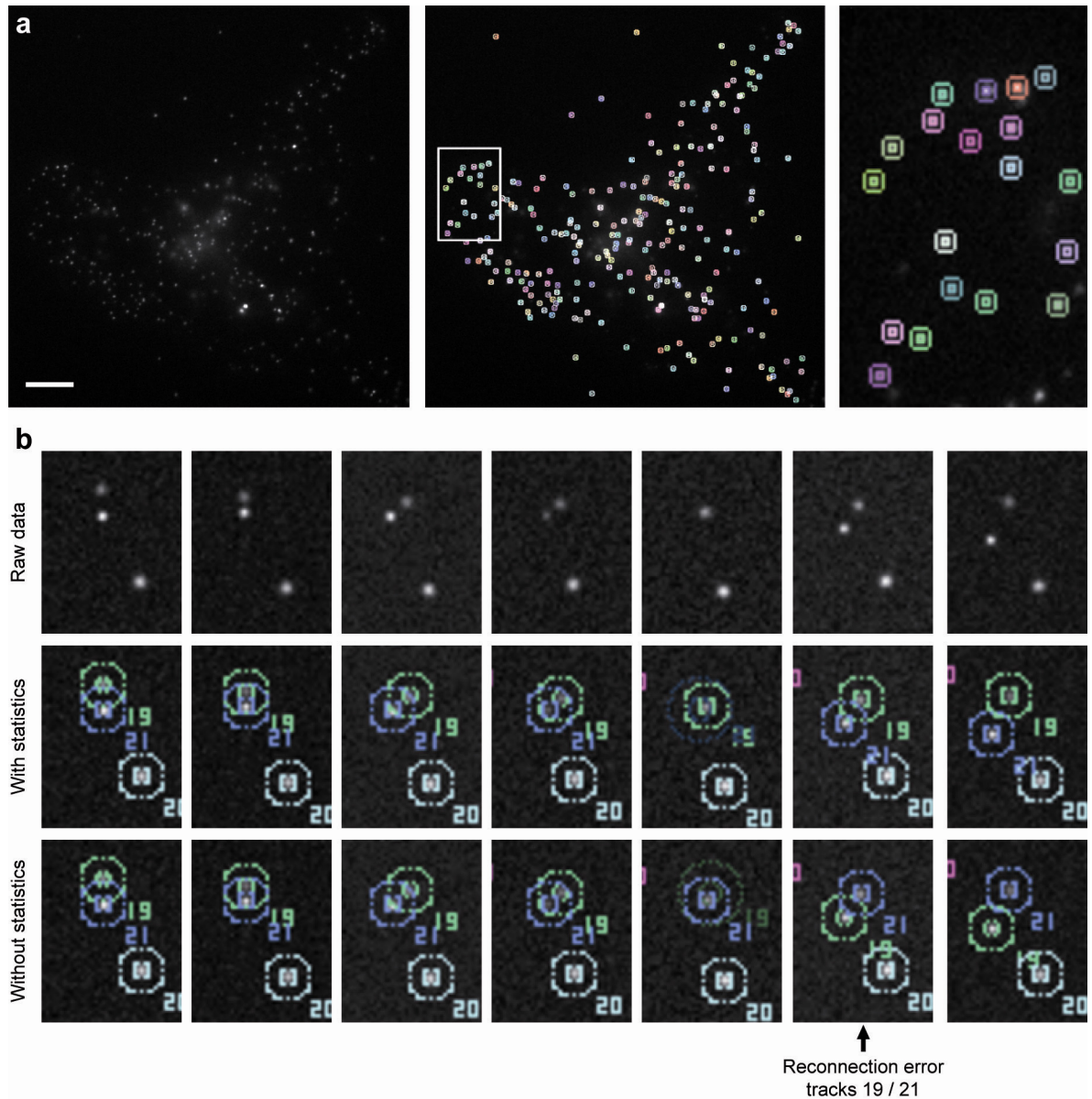
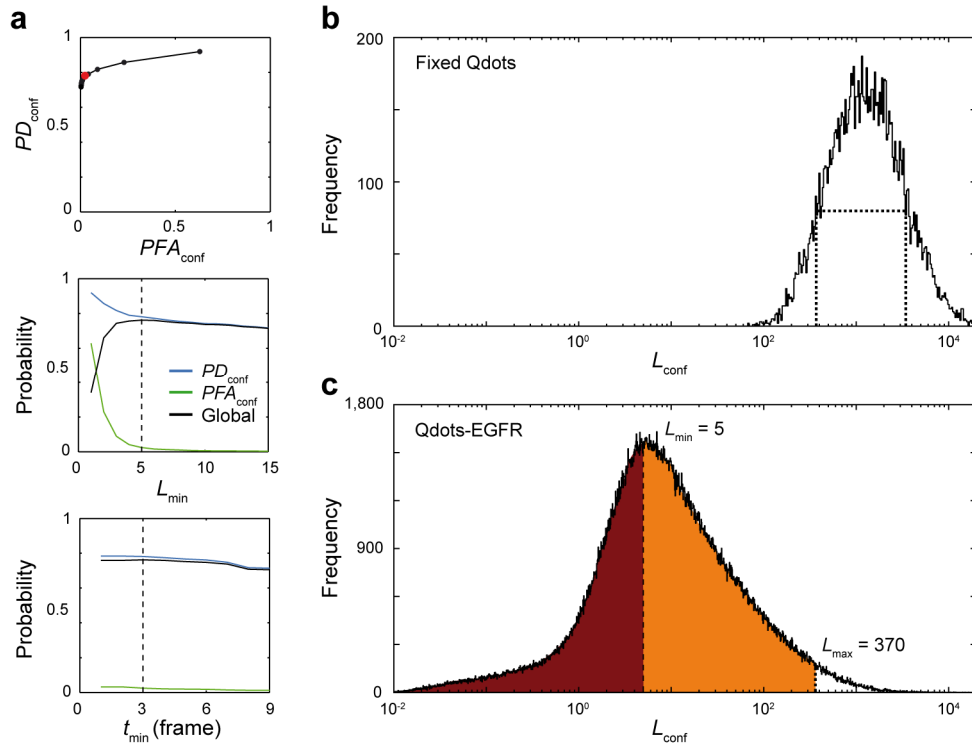


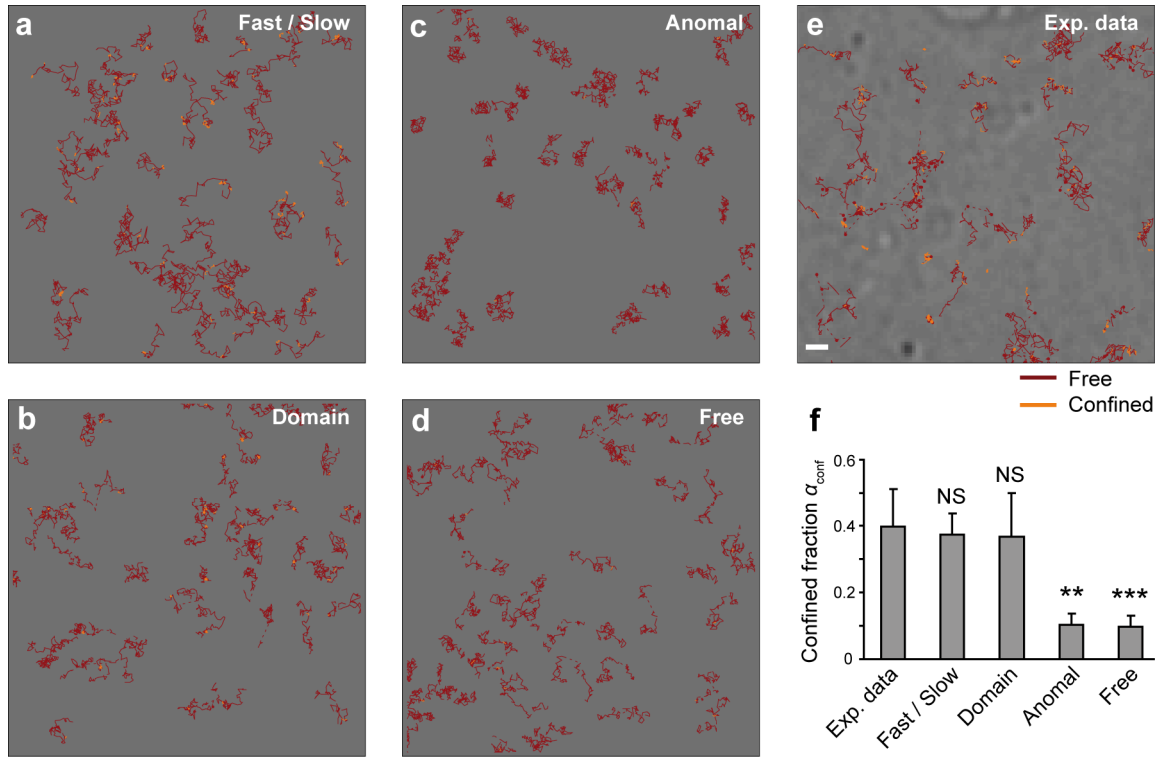
Illustration of MTT computation (a) Live COS-7 cells were labeled with 10 nM anti-EGFR-Qdot605 complexes (left). Qdots trajectories are reconnected using MTT (middle, see **Fig. 5c**). Pseudo-colours are used for clarity purpose. Scale bar, 10 μm . Right: zoom of the framed area, with concentric reconnection domains associated to local and maximal diffusion of each particle (corresponding to **Supplementary Video 1**) (b) Advantage of past statistics for reconnection. Simulated data (upper sequence) were reconnected using (middle sequence) or not (lower sequence) past statistics to handle reconnection test for crossing particles (overlapping reconnection domains, see **Fig. 3** and **Mathematical Appendix 2**). Larger and dimmer reconnection domains correspond to blinked particles. This exemplifies how the knowledge of past statistics helps to adequately resolve each track. This effect, mostly occurring at high density ($> 0.4\%$), requires a very complex scheme to be properly quantified. The number of detected errors overestimates the exact MTT performances. Nevertheless, the correctness of reconnection is globally improved, as illustrated.

Supplementary Figure 3



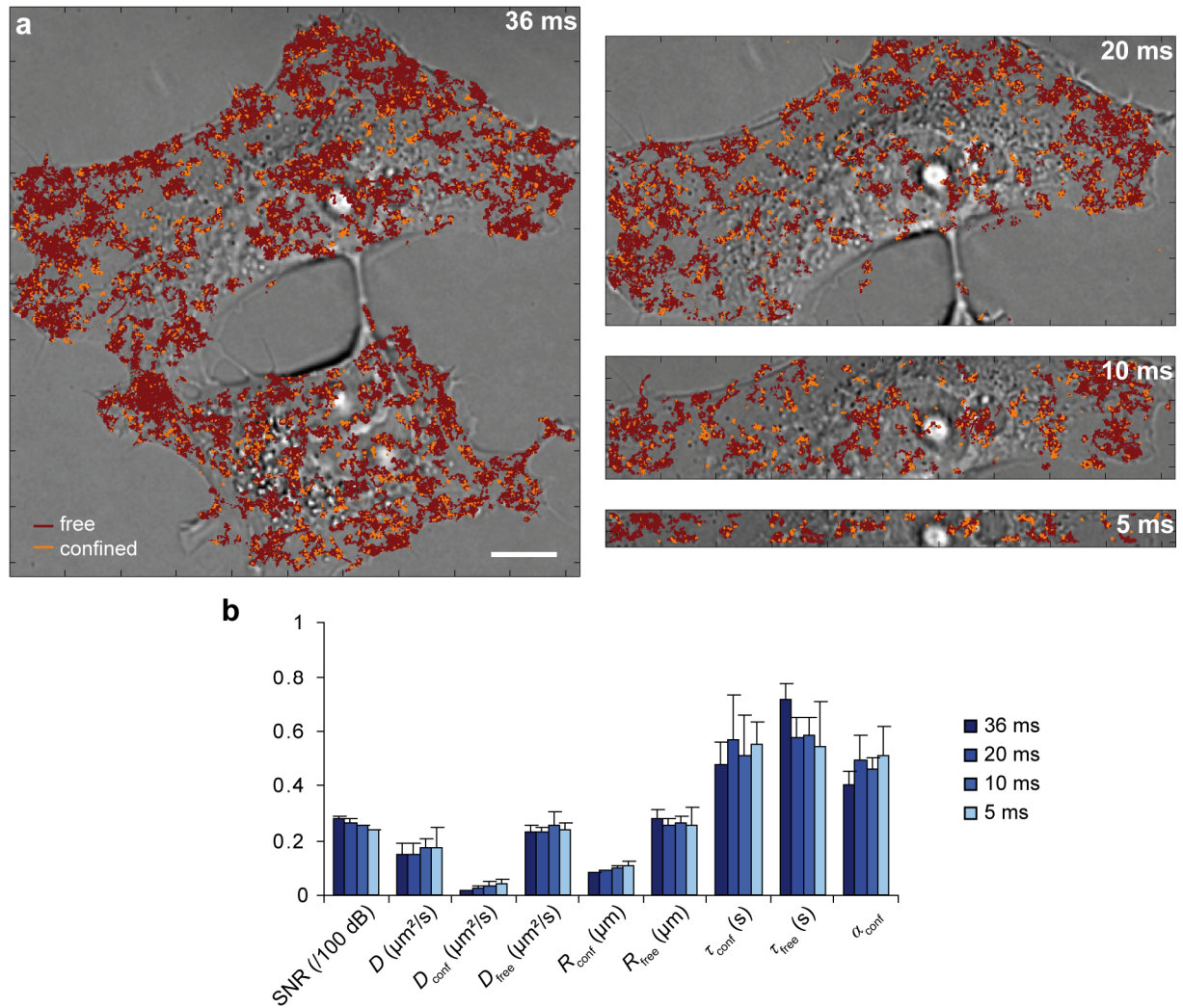
Confinement level calibration (a) ROC curve of PD_{conf} vs. PFA_{conf} (left) established from simulations by varying the threshold L_{min} ; the red dot represents the optimum. PD_{conf} (blue), PFA_{conf} (green) and global score (black) versus L_{min} (middle) and t_{min} (right) values. (b) Data from Qdots immobilized in Mowiol, a polymerizing resin commonly used as mounting medium¹, exhibiting a logarithmic bell shape-like distribution, located between 370 and 3,700 (values at half maximum, $n = 3$ samples). (c) Data from Qdots bound to EGFR on live cells ($n = 3$ cells). Minimum and maximum threshold values of confinement separate free (bordeaux, below L_{min} , as determined in **Fig. 5b**), confined (orange, between L_{min} and L_{max}) and immobile (white, above L_{max}) events, as illustrated.

Supplementary Figure 4



Evaluation of confinement models (a-e) Examples of simulated and experimental trajectories, with confinement encoded in orange, as in **Fig. 5**. Various types of confinement were simulated: **(a)** alternations of fast and slow events mimicking transient binding to rigid or slowly mobile structures (as used to optimize the confinement detection, see equation [3] and methods), **(b)** permeable domains with a radius of 0.7 pixel and a crossing probability of 0.1, placed on a square lattice of 2.5-pixel periodicity, and **(c)** anomalous diffusion, generated using $\langle r^2 \rangle = 4Dt^\gamma$, with an exponent $\gamma = 0.8$, which translates into correlating displacement². In all simulations, including free diffusion (absence of confinement for negative control, **d**), random walks were generated as described in methods, using uniform random initial positions. Each image measures 100×100 pixels and displays 50 trajectories of 100 steps. All parameters were set to best approximate experimental data **(e)**. Scale bar, 1 μm . **(f)** In the histogram, confinement was evaluated using the confined fraction α_{conf} . Experimental data ($n = 5$ cells) were compared with 4 different simulated datasets ($n = 50$ files). Statistical relevance: NS, non-significant ($P > 0.05$); **, $P < 0.01$; ***, $P < 0.001$ as calculated by Kruskal-Wallis test. All five conditions (including experimental data) were analyzed using the same confinement detection scheme.

Supplementary Figure 5



MTT at increased acquisition rate (a) Representative example of the same cells sequentially measured at decreasing exposure times, as indicated. With frame transfer cameras, exposure time is equal to acquisition time albeit the field of view may need to be reduced (down to 50 pixels for 5 ms exposure). Free parts are in bordeaux and confined parts in orange. Scale bar, 10 μm . **(b)** Quantification, depicting the overall stability of each parameter ($n = 5$ cells).

Supplementary Table 1

Glossary of fluorescence peak, trajectory and free & confined event descriptors

The last column (I/O) indicates if the parameter is either set before analysis (in) or evaluated (out) (and non relevant otherwise). In the second case, the indicated value corresponds to typical experimental results.

I. Fluorescence peak descriptors

symbol	definition of the parameter	value	I/O
d_{peak}	Peak density (% peaks per pixel)	$\sim 0.15\%$	out
G	bidimensional Gaussian (eq. [1] and Suppl. eq. [2]) normalized to a power of one ($P = \sum_n G_n^2 = 1$)	-	-
I	Particle fluorescence intensity (eq. [1])	-	out
$\langle I_{\text{on}} \rangle$	mean fluorescence intensity of non-blinking particles (full on state, Suppl. Fig. 1)	$\sim 11,000$ a.u.	out
i, j	pixel coordinates (eq. [1] and Suppl. eq. [2])	-	-
i_0, j_0	Gaussian center coordinates (eq. [1] and Suppl. eq. [2])	-	out
$\delta i_0, \delta j_0$	Localization accuracy (standard error on i_0, j_0 , Fig. 4b)	~ 6 nm	out
m	mean image offset (eq. [1], Suppl. Fig. 1)	$\sim 4,000$ a.u.	out
$N_{i,j}$	image noise at pixel (i, j) (eq. [1])	-	-
PD_{peak}	probability of peak detection	~ 1	in
PFA_{peak}	probability of false alarm (spurious peak detection)	10^{-6}	in
PFA_{orphan}	probability of false alarm for orphan peaks	10^{-7}	in
r_0	Gaussian radius (standard deviation) (Suppl. eq. [2])	~ 190 nm	out
σ	standard deviation of the noise (eq. [1])	~ 340 a.u.	out
SNR	signal to noise ratio: $SNR = 10 \text{ Log}(P / \sigma^2)$	~ 30 dB	out
w_s	spatial sliding window width used for particle detection	7 pixels	in
$X_{i,j}$	fluorescence intensity signal at pixel (i, j) (eq. [1])	-	in

II. Trajectory descriptors

symbol	definition of the parameter	value	I/O
D_{local}	local diffusion coefficient: $D_{\text{local}} \equiv r_{\text{local}}^2 / 4\tau$	$\sim 0.07 \mu\text{m}^2/\text{s}$	out
D_{max}	maximum diffusion coefficient: $D_{\text{max}} \equiv r_{\text{max}}^2 / 4\tau$ (unconstrained motion, upper limit of experimental data)	$0.2 \mu\text{m}^2/\text{s}$	in
N_{steps}	Trajectory length (# of frames, including blink)	~ 230 frames	out
P_{frame}	# of detected particles in the current image	~ 400	out
P_{domain}	# of detected particles in a reconnection domain (Fig. 3)	-	-
P_k	currently considered particle (Fig. 3)	-	-
r	spatial displacement between two successive frames	-	-
r_{local}	standard deviation of local steps between two successive frames: $r_{\text{local}} = \text{std}(r)$	~ 100 nm	out
r_{max}	maximum standard deviation of expected steps between two successive frames	170 nm	in
τ	acquisition time (= exposure time, using frame transfer)	36 ms	in
T_{frame}	# of reconnected trajectories up to frame t	~ 400 (up to 1,200)	out
T_{domain}	# of trajectories overlapping with a given reconnection domain (Fig. 3)	-	-
T_k	currently considered trajectory (Fig. 3)	-	-
τ_{off}	disappearance probability (exponential decay) for blinking	5 frames	in
w_t	temporal sliding window length for past statistics	5 frames	in

III. Free & confined event descriptors

symbol	definition of the parameter	value	I/O
α_{conf}	confined fraction (fraction of time spent confined) $\alpha_{\text{conf}} = \tau_{\text{conf}} / (\tau_{\text{conf}} + \tau_{\text{free}})$	0.40	out
D_{conf}	confined and free diffusion coefficient, resp. (fitted from the 5 first points of the MSD)	$0.007 \mu\text{m}^2/\text{s}$, $0.21 \mu\text{m}^2/\text{s}$	out
D_{min}	Minimum measurable diffusion coefficient	$2.5 \cdot 10^{-4} \mu\text{m}^2/\text{s}$	out
L_{conf}	confinement level (eq. [3] and Suppl. Fig. 3)	~ 8	out
L_{min}	minimum confinement level (lower limit before free diffusion, Suppl. Fig. 3)	5	in
L_{max}	maximum confinement level (upper limit of measurable mobility, Suppl. Fig. 3)	370	in
PD_{conf}	probability of detecting confinement (assessed as the fraction of confinement correctly detected in simulations)	0.78	in
PFA_{conf}	probability of false confinement alarm (same definition)	0.025	in
R_{conf}	confined and free event size, resp. (standard deviation of positions within each zone)	70 nm, 150 nm	out
τ_{conf}	confined and free event duration, resp.	250 ms, 280 ms	out
τ_{free}	minimum confined duration (Suppl. Fig. 3)	3 frames	in
VMR	Variance to mean ratio: $\text{var}(\text{Log}(L_{\text{conf}})) / \text{mean}(\text{Log}(L_{\text{conf}}))$	~ 0.1	out
w_{conf}	temporal sliding window length for confinement detection	4 frames	in

SUPPLEMENTARY METHODS

Monte Carlo simulations

Random walks were generated using homemade scripts. All parameters were set iteratively to match experimental data: input values were adjusted *a posteriori*, if required, according to the output. Each step was randomly distributed around a mean length $r = 2D^{1/2}$. Blinking probabilities of turning on and off were set to 0.3 and 0.08, respectively. Images were generated using diffraction-limited Gaussian peaks of 1-pixel radius (see Supplementary equation [2] in **Mathematical Appendix 2**). Fluorescence intensities followed a Gaussian distribution with a value of $11,000 \pm 1,000$ a.u. with 30 dB Gaussian noise, according to typical EM-CCD signals. Unless specified, density was set to a mean of 0.4% (40 peaks / 100×100 pixels). Confinement detection was optimized using simulations alternating between high and low diffusion coefficients: $D = 0.3$ or 0.006 pixel²/image, during 30 or 20 images on average for fast or slow periods, respectively. Diffusion values and durations follow Gaussian and exponential statistics, respectively.

Cell culture and Qdot staining

Biotinylated anti-EGFR Ab-3 antibody (Lab Vision) was mixed with streptavidine-Qdot605 (Ozyme) in the presence of 100× excess of biotin in order to achieve a single mAb per Qdot. Complexes were incubated for 15 min on COS-7 cells (ATCC) before washing out unbound Qdots (3 times in HBSS, 10 mM HEPES buffer) and imaging. Using 10 nM antibody-Qdots led to a range of 300 to 500 labeled receptors per cell (**Supplementary Fig. 1**). For control, Qdots were immobilized in Mowiol mounting medium¹ which is a polymerizing resin commonly used for cytochemistry with fixed cells. The measured diffusion coefficient D_{\min} was in agreement with the associated confinement level, assuming the formal relation $L_{\text{conf}} \approx D_{\text{global}} / D_{\text{local}}$ with $D_{\text{local}} \approx \text{var}(r) / w_{\text{conf}}$. This value was consistent with the lower limit expected for immobile particles, according to the localization accuracy δi_0 :

$$D_{\min} = D_{\text{global}} / \langle L_{\text{conf}} \rangle = \delta i_0^2 / 4\tau = 2.5 \cdot 10^{-4} \mu\text{m}^2/\text{s}$$

Equipment and settings

Samples were imaged at 37°C on an Axiovert 200M microscope (Zeiss) using a FluoArc HBO 100 W lamp, a 100× 1.45 NA objective and FF01-457/50 excitation, FF495-Di02 dichroic, and FF01-617/73 emission filters (Semrock). Frame grabbing was done using a 16-bit EM CCD Cascade 512 BFT camera (Roper Scientific) with the amplification gain set at 3850 to avoid saturation. A

DIC image of the cell was taken before recording stacks. Unless noted, each stack typically consisted of 300 images, taken using frame transfer at $\tau = 36$ ms, in full frame (512×512 pixels). For image display, particles with confinement comparable to immobilized Qdots were discarded as non-informative data (**Supplementary Fig. 3**).

SUPPLEMENTARY NOTE

MTT Algorithm Principle

Within the framework of the statistical theory of image processing, the algorithm must rebuild trajectories of numerous diffusing particles, starting from a stack of fluorescence images (see **Supplementary Video 1**). A global method would involve a multi-hypotheses analysis: evaluation of a whole stack at once, simultaneously handling detections and reconnections for all frames, together with the associated estimations of each parameter (i.e. position, intensity). Besides requiring a substantial computing time, such a problem is also extremely complex to solve. Using a pragmatic approach, we have been able to overcome these issues.

As summarized in the synopsis below, MTT is intended to run over stacks of images acquired by video-microscopy. The overall data evaluation follows 3 major steps: particle detection within each image, evaluation of the relevant peak characteristics and finally reconnection of positions, through time, to reconstitute trajectories.

Starting from the first image, fluorescent peaks are detected by a test of hypotheses (**Appendix 1**). This initiates beginning trajectories. Each peak is further characterized by estimating parameters such as position and intensity. For each parameter, we computed the CRB limit in order to delineate the theoretical performances such as the subpixel accuracy (**Appendix 4**). For each frame, performing deflation allows to avoid missing particles of lower intensity when they are hidden by a neighboring one of stronger intensity.

This process is then iterated over the whole stack, in order to reconnect the trajectories frame by frame. The association test takes into account past statistics for diffusion, intensity and blinking (**Appendix 2**). Potential new trajectories are validated or not using a more stringent detection test.

One major goal of MTT is to be robust even at high labeling densities in order to allow extensive investigations of molecular dynamics (**Appendix 3**). The resulting data can be further processed for

relevant dynamic descriptors, such as confinement, as presented in this study.

In classical SPT, misconceptions mainly come from a bias that usually favors the nearest neighbor and not the fastest particles. Although this issue is even more crucial at high particle density, we were able to significantly reduce errors by introducing both the deflation and integrated historical information reconnection modules.

MTT algorithm overview

The following lines summarize the main steps performed by the algorithm:

1. First iteration (first image of the stack)
 - 1.1. Detection and estimation, deflation loop
 - Detection map
 - Estimation of the peaks
 - Subtraction of the detected peaks from the image
2. Loop over the images
 - 2.1. Detection and estimation, deflation loop
 - Detection map
 - Estimation of the peaks
 - Subtraction of the detected peaks from the current image
 - 2.2. Reconnection of the peaks found in the current image
 - 2.2.1. Loop over trajectories, from on trajectories to oldest blinked
 - Selection of the set of trajectories and particles in competition
 - Reconnection test
 - Reset of the trajectories blinked for too long
 - Update of the estimated parameters and associated statistics
 - 2.2.2. Creation of new trajectories from validated orphan peaks
 - 2.2.3. Update of the data
3. Backup of the data (tables of parameters, means and variances)
4. Further analyses (i.e. confinement evaluation and mapping)

Tutorial of Signal Detection Concepts

Signal detection ultimately aims at discriminating a relevant signal (such as fluorescence here) from background noise. Several concepts and dedicated tools have been developed by the community and employed in the present work, allowing us to achieve efficient and accurate detection of individual Qdot signals within our live cell experimental acquisitions^{3,4}.

Signal-to-noise ratio (SNR) is defined as the ratio of a signal power (square intensity I^2) to the noise power (variance σ^2) corrupting the signal. Contrarily to a fluctuating component (of standard deviation σ), a constant background (offset m) will not affect the SNR, thus the measurement. The higher the ratio, the less obtrusive the background noise is, hence the easier the estimation of the signal. Because many signals have a very wide dynamic range, SNR is usually more adequately expressed using the logarithmic decibel scale. In decibels, the SNR is, by definition, 10 times the decimal logarithm of the power ratio:

$$SNR = 10 \text{ Log}(I^2 / \sigma^2).$$

Given the typical signal and noise measured in our data, $I \approx 11,000$ a.u. and $\sigma \approx 340$ a.u. leads to $SNR \approx 30$ dB. This value, corresponding to non blinking Qdots, allows very accurate sub-pixel localization. Note that when considering the raw pixel values, average peak amplitude is equal to $I/\pi^{1/2}r_0 \approx 5000$ a.u., with $r_0 \approx 1.2$ pixels (see Supplementary equation [2]). An alternate definition of the signal-to-noise ratio can be the ratio between average peak amplitudes $I/\pi^{1/2}r_0$ and noise level σ , as would be observed from a line-scan through an image. In the present case, this amplitude ratio leads to $I/\pi^{1/2}r_0\sigma \approx 15$. Similarly, for the detection limit, $SNR \approx 20$ dB corresponds to an amplitude ratio of ~ 5 .

Maximum likelihood (ML) estimation is a popular statistical method used for fitting a mathematical model to experimental noisy data or randomly fluctuating data. Modeling data by estimating ML offers a way of tuning the free parameters of the model to provide an accurate fit. The method was pioneered by Sir R. A. Fisher, with widespread applications for testing hypotheses. The method of ML corresponds to many well-known estimation methods in statistics. For a fixed set of data and underlying probability model, ML determines the values of the model parameters that describe the data better than any other values. ML corresponds to a least square fit in the case of Gaussian noise. In MTT, ML is first used for peak detection, to evaluate the respective likelihood of having either a peak or only noise within the search window. ML is also used to reconnect trajectories, by estimating the likelihood of all relevant peak-trajectory combinations.

The **generalized likelihood ratio test (GLRT)** is a statistical test for making a decision between two different hypotheses. The likelihood ratio test (LRT) is based on the value of the ratio of the maximum probability of a result under the two hypotheses. In most cases, the exact value of the parameters corresponding to specific hypotheses is unknown. Computing a numerical ML estimate

then provides a generalized test, as performed in MTT, for peak detection.

Constant false alarm rate (CFAR) detection refers to a form of adaptive algorithm used to detect targets against a background of noise. The role of the CFAR is to determine the threshold above which any signal can be statistically considered not to originate from the noise. Even with no target, there is always a remaining probability, the PFA , for the noise to overpass any threshold. The goal of a CFAR detector is to control this probability. In most detectors, the threshold is set in order to achieve a required, constant PFA , which further sets the threshold. If the background is constant in time and space, then a fixed threshold can be chosen that provides a specified PFA , only governed by the probability density function of the GLRT. The PD is then a function of the SNR of the targets. However, in most systems, the noise and background levels may change both spatially and temporally. This typically holds for cellular autofluorescence for instance. In this case, a local search window is used, as in the present work for instance. Thus, for MTT, we choose a PFA_{peak} inversely related to the number of pixels (i.e. 10^{-6}). This ensures that, in average, less than one spurious detection (noisy peak “accidentally” detected) can arise.

The **Fisher information**, developed by the geneticist and statistician Sir R. A. Fisher, is a way of measuring the amount of information that an observable random variable X (here, a fluorescence image depicting particles and noise) carries about an unknown parameter θ upon which the likelihood function of θ , $L(\theta) = f(X; \theta)$, depends. The Fisher information is not a function of a particular observation, as the random variable X has been averaged out. The concept of information is useful when comparing two methods of observing a given random process.

When there are n parameters, so that θ is a n by 1 vector (as in the present case, with 6 parameters for the Gaussian used for approximating the peaks), then the Fisher information takes the form of an n by n matrix.

The **Cramér–Rao bound (CRB)**, named in honor of H. Cramér and C. R. Rao, expresses a lower bound on the variance of estimators of a deterministic parameter. In its simplest form, the bound states that the variance of any unbiased estimator is at least as high as the inverse of the Fisher information. An unbiased estimator which achieves this lower bound is said to be efficient. Such a solution achieves the lowest possible mean squared error among all unbiased methods, and is therefore the minimum variance unbiased (MVU) estimator. The Cramér–Rao bound can also be used to bound the variance of biased estimators. In the

present work, computing the Fisher matrix and the associated CRB allowed us to estimate the theoretical lowest error expected for each peak parameter, the most relevant of them being the positional accuracy δi_0 , since it directly relates to the tracing accuracy.

The **receiver operating characteristic (ROC)** analysis provides tools to select possibly optimal models and to discard suboptimal ones independently from (and prior to specifying) the cost context or the class distribution. ROC analysis is related in a direct and natural way to cost/benefit analysis of diagnostic decision making. ROC consists in a graphical plot of PD vs. PFA as the threshold varies. Because of inherent noise, evaluating any parameter with an absolute precision is impossible. There is always an ultimate limit, which is the CRB. In the present work, the ROC provided us with an objective approach to set the threshold values used to detect confinement, namely L_{\min} and t_{\min} .

Mathematical Appendix 1

Detection of Gaussian particles by test of hypotheses

The detection algorithm implemented is based on the following mathematical development: Two hypotheses H_0 and H_1 are compared, where H_0 defines the non-presence of particles and H_1 the presence of a particle. These two hypotheses are defined as depicted in **Fig. 2a**, assuming Gaussian noise. The detection described below uses a GLRT corresponding to a LRT from which the parameters are analytically estimated by ML and then reintroduced.

H_0 hypothesis: no target

H_0 is defined in the following way:

$$X_n = m + N_n$$

where m corresponds to the offset and N to a Gaussian noise of variance σ^2 .

$n = (i, j)$ is a spatial variable corresponding to a position inside the considered bidimensional window of size w_s : $i, j \in [1, w_s]^2$

Let L be the log-likelihood of the H_0 hypothesis:

$$L(H_0|m, \sigma^2) = -(w_s^2/2) \ln(2\pi\sigma^2) - (1/2\sigma^2) \sum_n (X_n - m)^2$$

where σ^2 and m are unknown. To determine them, we firstly compute the partial derivative of L with respect to σ^2 :

$$\partial L_{H_0} / \partial \sigma^2 = 0 \Rightarrow \hat{\sigma}_0^2 = (1/w_s^2) \sum_n (X_n - m)^2$$

$$L(H_0|m, \hat{\sigma}_0^2(m)) = -(w_s^2/2) \ln(2\pi \hat{\sigma}_0^2) - w_s^2/2$$

We then take the partial derivative of L with respect to m :

$$\partial L(H_0|m, \hat{\sigma}_0^2(m)) / \partial m = 0 \Rightarrow \hat{m} = (1/w_s^2) \sum_n X_n$$

This leads to the ML estimate:

$$L(H_0 | \hat{m}, \hat{\sigma}_0^2 (\hat{m})) = -(w_s^2/2) \ln(2\pi \hat{\sigma}_0^2 (\hat{m})) - w_s^2/2 \quad [1]$$

$$\begin{aligned} \text{Remark: } \hat{\sigma}_0^2 (\hat{m}) &= (1/w_s^2) \sum_n (X_n - \hat{m})^2 \\ &= (1/w_s^2) \left(\sum_n X_n^2 \right) - \hat{m}^2 \end{aligned}$$

H_1 hypothesis: presence of a target in the center of the window

H_1 is written:

$$X_n = I \times G_n + m + N_n$$

where m corresponds to the offset and N to a Gaussian noise of variance σ^2 as before. In addition, a Gaussian G (modeling the microscope PSF) weighted by an intensity I is located in (i_0, j_0) , coordinates of the center of the window, with a radius r_0 and is normalized to a power (squared signal) of one:

$$G_{ij}(i_0, j_0, r_0) = 1/(\pi^{1/2} r_0) \exp(-(i-i_0)^2 + (j-j_0)^2)/2r_0^2) \quad [2]$$

Setup characteristics ensure that r_0 is slightly higher than one pixel, thus satisfying adequate sampling according to the Nyquist-Shannon theorem.

The estimate here is equal to:

$$L(H_1 | m, \sigma^2, I) = -(w_s^2/2) \ln(2\pi\sigma^2) - (1/2\sigma^2) \sum_n (X_n - m - IG_n)^2$$

This time there are three unknowns: σ^2 , m and I . Following the same method as for H_0 , one finds:

$$\hat{\sigma}_1^2 = (1/w_s^2) \sum_n (X_n - m - IG_n)^2$$

$$\Rightarrow L(H_1 | m, \hat{\sigma}_1^2 (m), I) = -(w_s^2/2) \ln(2\pi \hat{\sigma}_1^2) - w_s^2/2$$

The minimum of L corresponds to the maximum of $\hat{\sigma}_1^2(I, \hat{m}_1(I))$.

Therefore, derivating $\hat{\sigma}_1^2$ allows estimating m and I :

$$\partial \hat{\sigma}_1^2 / \partial m = 0 \Rightarrow \hat{m}_1(I) = (1/w_s^2) \sum_n (X_n - IG_n)^2$$

$$\begin{aligned} \hat{\sigma}_1^2 &= (1/w_s^2) \sum_n \left(X_n - IG_n - (1/w_s^2) \sum_n (X_n - IG_n)^2 \right)^2 \\ &= (1/w_s^2) \sum_n \left(X_n - \hat{m}_0 - I \left(g_n - (1/w_s^2) \sum_n G_n \right) \right)^2 \end{aligned}$$

Let $\tilde{X} = X - \hat{m}$ and $\tilde{G} = G - (1/w_s^2) \sum_n G_n$ be the

centered image and Gaussian counterparts.

$$\Rightarrow \hat{\sigma}_1^2 = (1/w_s^2) \sum_n (\tilde{X}_n - I \tilde{G}_n)^2$$

We determine I accordingly:

$$\begin{aligned} \partial \hat{\sigma}_1^2 / \partial I &= 0 \Rightarrow \sum_n (\tilde{X}_n - I \tilde{G}_n)^2 = 0 \\ \Rightarrow \hat{I} &= \sum_n \tilde{X}_n \tilde{G}_n / \sum_n \tilde{G}_n^2 \end{aligned}$$

Note that

$$\hat{I} = \sum_n \tilde{G}_n (X_n - \hat{m}) / \sum_n \tilde{G}_n^2 = \sum_n \tilde{G}_n X_n / \sum_n \tilde{G}_n^2.$$

Finally,

$$\begin{aligned} \hat{\sigma}_1^2 &= (1/w_s^2) \left(\sum_n \tilde{X}_n^2 + \sum_n \hat{I}^2 \tilde{G}_n^2 - 2 \sum_n \hat{X}_n \hat{I} \tilde{G}_n \right) \\ &= (1/w_s^2) \sum_n \tilde{X}_n^2 - \sum_n \tilde{G}_n^2 \\ &= \hat{\sigma}_0^2 - (1/w_s^2) \hat{I}^2 \sum_n \tilde{G}_n^2 \end{aligned}$$

$$\text{with } \hat{I} = \sum_n \tilde{G}_n X_n / \sum_n \tilde{G}_n^2$$

$$\text{and } L(H_1 | \hat{m}, \hat{\sigma}_1^2, \hat{I}) = -(w_s^2/2) \ln(2\pi \hat{\sigma}_1^2) - w_s^2/2 \quad [3]$$

Hypothesis map H_0/H_1

The hypothesis map used as detection plane is obtained from the difference between the estimates of H_0 and H_1 . It leads to a plane with very sharp peaks corresponding to the estimate made on the entire image.

$$c = L(H_0) - L(H_1)$$

$$\begin{aligned} &= -(w_s^2/2) \ln(\hat{\sigma}_0^2 / \hat{\sigma}_1^2) \\ &= (w_s^2/2) \ln(\hat{\sigma}_1^2 / \hat{\sigma}_0^2) \\ &= (w_s^2/2) \ln \left(1 - \left(\hat{I} / w_s \hat{\sigma}_0 \right)^2 \sum_n \tilde{G}_n^2 \right) \\ &= (w_s^2/2) \ln \left(1 - \hat{I}^2 \sum_n \tilde{G}_n^2 / \left(\sum_n X_n^2 - w_s^2 \hat{m}^2 \right) \right) \quad [4] \end{aligned}$$

Detection at Constant False Alarm Rate (CFAR)

H_0 becomes false if

$$-2(L(H_0) - L(H_1)) > \chi^2(n_1 - n_0)$$

where n_1 is the number of unknown factors in the problem and χ is the detection threshold.

$n_1 - n_0 = 3 - 2 = 1$ because $n_1 = [m; \sigma^2; I]$ and

$n_0 = [m; \sigma^2]$.

One determines χ^2 for a given fixed PFA : for instance, $\chi^2 = 24$ corresponds to $PFA \approx 10^{-6}$. Note that the exact correspondence between χ^2 values and the associated PFA is strictly known only for large spatial windows and/or low noise. However, in all cases, χ^2 only has to be optimized once when calibrating the algorithm for a given dataset^{3,4}.

Estimation of detected peaks

Estimation is carried out using the ML method (the optimization of the Supplementary equation [3] corresponding in this case to a classical minimum mean square error fit), under the assumption of independent identically distributed Gaussian noise. Optimization is performed by Gauss-Newton regression using analytical expressions of the first and second derivatives^{3,4}. We therefore minimize the following expression by a least squares analysis:

$$(\hat{I}, \hat{i}_0, \hat{j}_0, \hat{r}_0, \hat{m}) = \arg \min_{I, i_0, j_0, r_0, m} \sum_{i,j} (X_{i,j} - I \times G_{i,j}(i_0, j_0, r_0) - m)^2 \quad [5]$$

The expression used for the Gaussian (Supplementary equation [2]) is the same for detection and estimation. However, the parameters

are changing between the two steps: for detection, the coordinates of the center (i_0, j_0) are integer pixel values and the radius r_0 is fixed to a default value (1.1 pixel) while for estimation, the values of all three parameters are refined with sub-pixel accuracy.

Mathematical Appendix 2

Probability laws and reconnection test

For the reconnection step, three descriptors are used to help attributing the relevant peaks to their trajectories: diffusion, intensity and blinking. The likelihood that a given trajectory T_i matches with a given particle P_j is estimated with probability laws which are evaluated using the previous and current frames, respectively. The product of the three corresponding probabilities provides the test evaluating such reconnection.

Probability law for diffusion

For $r < 3r_{\max}$,

$$\begin{aligned} p_{\text{diff}}(r) &= \gamma_{\text{diff}} p_{\text{local}}(r) + (1 - \gamma_{\text{diff}}) p_{\text{max}}(r) \\ &= \gamma_{\text{diff}} / (\sqrt{2\pi} r_{\text{local}}) \exp(-r^2 / 2r_{\text{local}}^2) \\ &\quad + (1 - \gamma_{\text{diff}}) / (\sqrt{2\pi} r_{\text{max}}) \exp(-r^2 / 2r_{\text{max}}^2) \end{aligned}$$

and $p_{\text{diff}}(r) = 0$ otherwise

The probability for a given particle to move along a displacement r between two successive frames is given by the mixing of two Gaussian laws, both centered at the current position at time t , but with different standard deviations. The first term corresponds to local diffusion D_{local} , as defined by a Gaussian law with standard deviation r_{local} (still allowing possible slow down). r_{local} is estimated and updated by evaluating D_{local} within the temporal window w_t (hence from the 5 previous frames). A significant weight γ_{diff} (set to 0.9) statistically emphasizes on the local behavior, without completely excluding the possibility of a sudden increase towards free diffusion. The second term accounts for such possible accelerations, upper bounded by a standard deviation r_{max} , with $r_{\text{max}} > r_{\text{local}}$. A correspondingly lower weight $(1 - \gamma_{\text{diff}})$ accounts for a reduced probability.

Probability law for intensity

$$\begin{aligned} p_{\text{int}}(I) &= \gamma_{\text{int}} p_{\text{on}}(I) + (1 - \gamma_{\text{int}}) p_{\text{blink}}(I) \\ &= \gamma_{\text{int}} / (\sqrt{2\pi} \sigma_I) \exp(-(I - \langle I_{\text{on}} \rangle)^2 / 2\sigma_I^2) \\ &\quad + \{(1 - \gamma_{\text{int}}) / \langle I_{\text{on}} \rangle\} \chi_{I \in [0, \langle I_{\text{on}} \rangle]} \end{aligned}$$

$\langle I_{\text{on}} \rangle$ is the mean fluorescence intensity and σ_I is the corresponding standard deviation. The first term, Gaussian, accounts for non-blinking qdots, and the second, constant between 0 and $\langle I_{\text{on}} \rangle$, corresponds to fast blink (Supplementary Fig. 1). According to data evaluation, both cases appear to

have comparable probabilities, thus γ_{blink} is set in first approximation to 1/2.

Note that the full probability law cannot be reliably evaluated within the window w_t . Thus, to evaluate and update its two parameters $\langle I_{\text{on}} \rangle$ and σ_I , the two cases (on or blink) are first discriminated by a generalized likelihood ratio test (GLRT). The parameters are then evaluated only if the particle is detected in the on state ($p_{\text{on}} > p_{\text{blink}}$). Otherwise, as long as the particle is statistically detected in the blinking state, the parameters are not updated.

Besides, the 3rd blink issue, full off (see below), corresponds to no detected intensity. This null intensity could be formally stated in the statistical law as a Dirac centered at zero, but without providing any further information.

Probability law for full blink/disappearance

$p_{\text{off}}(t) = 1$ for all detected particles in the last frame (either in the full on or fast blink state)

$p_{\text{off}}(t) = \exp(-(t - t_{\text{off}}) / \tau_{\text{off}})$ for blinking, previously detected particles (thus in the full off state since time t_{off}) and

$p_{\text{off}}(t) = 0$ if $t - t_{\text{on}} > 3\tau_{\text{off}}$ (with $3\tau_{\text{off}}$ estimated at 15 frames) for long-lasting off states.

This law traduces the probability for a blinked particle (full off) to reappear at time $t+1$ (above the detection limit: either as full on or fast blink). It is thus only relevant for off (fully blinked) particles. Since blinking can occur on any time-scale, this is expressed by an exponential decay, reducing accordingly their statistical weight in the combinatory test. For long-lasting blink, a cutoff at $3\tau_{\text{off}}$ permits the definitive ending of the trajectory (by annulling the reconnection probability), to avoid irrelevant combinatorial complexity.

ML test for reconnection

$p_{\text{rec}} = \prod_{i,j} L(T_i, P_j)$ is the probability associated to a

given association set (T_i, P_j) (see Fig. 3c) with $L(T_i, P_j) = p_{\text{diff}}(r) \cdot p_{\text{int}}(I) \cdot p_{\text{off}}(t)$ evaluated for each combination (i, j) , using past statistics from trajectory T_i and current parameters of particle P_j . Through this operation, all the information (position, mobility, intensity and blink) can be integrated for the reconnection decision.

The log-likelihood function is thus equal to:

$$\begin{aligned} \log(p_{\text{rec}}) &= \sum_{i,j} \log(L(T_i, P_j)) \\ &= \log(p_{\text{diff}}(r)) + \log(p_{\text{int}}(I)) + \log(p_{\text{off}}(t)) \end{aligned}$$

Each trajectory is tested for association with each particle within its reconnection domain. If necessary, this includes $T_i = \text{off}$ (particle turned or remained in the off state) and/or $P_j = \text{new}$ (possible initiation of a new trajectory, thus assigned with the

default statistical values for the subsequent frames) (see **Fig. 3c**). The retained combination is the one which maximizes this global probability (according to available descriptors, in other studies, alternative probabilistic scores have also been used for reconnection⁵). Trajectories are classified according to their blinking history: they are tested starting from the oldest on to the oldest off. The latter is limited by the cutoff fixed at $3\tau_{\text{off}}$.

Mathematical Appendix 3

MTT efficiency versus particle density

MTT is designed to face high densities of labeling. Hence, establishing the density limits is critical to benchmark its performances. In particular, detection is mostly limited by particle colocalization, which in turns is directly linked to density. This holds also for reconnection, taking into account particles diffusion. Conversely, investigating confinement led to the notion of area revisits, which also relate do density.

Particle colocalization probability

Our analyses allow peaks of radius $r_0 \approx 190$ nm (1.2 pixels) to be localized with sub-pixel accuracy: $\delta i_0 \approx 6$ nm (0.04 pixel) for typical SNR, with at least $\delta i_0 \approx 16$ nm (0.1 pixel) guaranteed (**Fig. 4b**)^{6,7}. This radius is higher than the theoretical size of diffraction-limited peaks, one third of the Airy radius⁸:

$r_{\text{PSF}} = r_{\text{Airy}} / 3 = 0.61\lambda / 3NA = 85$ nm (0.53 pixel) for Qdots emitting at 605 nm.

The difference between measured and theoretical values may be accounted for by diffusion occurring during each observation (as well as by possible bias during radius estimation or by occasional out of focus particles). Indeed, during $\tau = 36$ ms, particles move on average

$$r_{\text{local}} = (4D_{\text{local}} \tau)^{1/2} \approx 100 \text{ nm (0.62 pixel)}$$

leading to $r_0 \approx r_{\text{PSF}} + r_{\text{local}}$. The Gaussian G of radius r_0 corresponds to a generalized transfer function, including optics (PSF) and blurring due to movement.

For reasonable values of SNR and density, the detection is almost complete (typically $\sim 95\%$, as quantified in **Fig. 4a**). As density increases, errors can arise either during detection, due to colocalization (relevant or fortuitous), or during reconnection, due to crossing trajectories. Indeed, missed detections mostly correspond to colocalized peaks (in the sense of optic resolution). Thus, Gaussian peaks of standard deviation r_0 must be separated by at least $3r_0 \approx 570$ nm (3.6 pixels).

For reasonably low densities, the probability of random colocalization is equal to the ratio of the elementary surface occupied by each peak, s_{peak} and the average available surface per peak, $\langle S \rangle$. The elementary peak surface corresponds to the Airy disk, corrected to include mobility during

acquisition (see above). This can be approximated to an elementary disk of radius $3r_0/2$:

$$s_{\text{peak}} = \pi (3r_0/2)^2 \approx 0.26 \mu\text{m}^2 \text{ (10 pixels}^2\text{)}$$

corresponding to a maximal density:

$$d_{\text{max}} = 1/s_{\text{peak}} \approx 4 \text{ peaks}/\mu\text{m}^2$$

$$(10\% = 10 \text{ peaks} / 10 \times 10 \text{ pixels})$$

This density can be interpreted as the asymptotical upper limit for resolving single molecules. Above this density, fluorescent peaks are statistically overlapping, leading to a homogenous staining as classically obtained by immunolabeling for instance. This limit remains much higher than the typical experimental densities used for MTT, $d_{\text{peak}} \approx 0.06 \text{ peak}/\mu\text{m}^2$ (0.15%). Even taking into account the fraction of the image filled by a cell would only moderately affect density (i.e. up to $0.12 \text{ peak}/\mu\text{m}^2$ for a cell occupying half of the image).

The available surface is the ratio of the total surface ($S_{\text{tot}} = 512 \times 512$ pixels) and the number of peaks ($P_{\text{frame}} \approx 400$), hence the inverse of the peak density:

$$\langle S \rangle = S_{\text{tot}} / P_{\text{frame}} = 1 / d_{\text{peak}}$$

Finally, $p_{\text{coloc}} = s_{\text{peak}} / \langle S \rangle = s_{\text{peak}} d_{\text{peak}} \approx 0.015$

Therefore, for the typical experimental labeling densities, only 1.5% of the particles are expected to be colocalized. Note that, whether random or not, colocalized peaks would appear as one single peak of approximately double intensity. This could be treated by stoichiometric analysis, though this is beyond the scope of the present work. The theoretical resolution limit of the current algorithm is thus related to an extended version of the Rayleigh criterion (two peaks separated by at least $3r_0 \approx 570$ nm, including again blurring). Therefore, excluding blinking probabilities, we obtain the following theoretical limit for detection performances:

$$\text{Detection score} \approx 1 - p_{\text{coloc}}$$

As can be easily deduced, this exhaustivity is directly linked to the reconnection efficiency: indeed, although blinking events have been taken into account, every missed peak can potentially lead to a break in the connection process (as a false negative detection), resulting in two shortened rather than one single trajectory. This becomes even more crucial when misdetection occurs while molecules are crossing, resulting in further putative errors in resolving each correct path. Thus, when implementing deflation, and providing sufficient SNR, only molecules crossing at a distance smaller than the detection limit can be misdetected. This is handled as described (**Fig. 3**), though for typical diffusion values, even as high as $1 \mu\text{m}^2/\text{s}$, and typical (single-molecule) labeling densities, this remains a rare event.

Pixel revisit probability

Accordingly, the probability to revisit a given pixel, when considering P_{frame} particles moving through N_{steps} random positions (mean trace length being ~ 230 frames), would be given by the ratio between the elementary pixel size $s_{\text{pixel}} = 1 \text{ pixel}^2$ and the average surface per particle integrated over time $\langle S \rangle$. For Brownian motion, the probability to revisit a given pixel gets high if the pixel size is comparable or bigger than the average displacement by frame. Hence, to circumvent this bias, revisits due to the same confined event are counted only once. Then, if confined events are separated enough in space and time, the bias will be notably reduced. In a first approximation, the probabilities can thus be assumed as independent.

$\langle S \rangle = S_{\text{tot}} / (P_{\text{frame}} N_{\text{steps}}) = 1 / (d_{\text{peak}} N_{\text{steps}})$
 leading to $p_{\text{revisit}} = s_{\text{pixel}} / \langle S \rangle = d_{\text{peak}} N_{\text{steps}} \approx 0.35$
 The probability of revisiting n times the same pixel is then

$$p_{n \text{ revisits}} = p_{\text{revisit}}^n$$

which is rapidly decreasing ($p_{5 \text{ revisits}} < 0.01$ for instance). This demonstrates that, in a random situation, observing frequent revisits of the same pixel is getting highly unexpected, establishing the statistical validity of the revisit map depicted in **Fig. 6c**. This was further assessed by computing revisit maps using simulations. Free diffusion mostly led to revisit numbers lower than 5 for a stack of 1,000 frames. Conversely, in the presence of domains, revisits were often significantly higher (not shown). We thus set 5 revisits as a threshold above which revisiting the same pixel becomes statistically relevant. In conclusion, this analysis requires high density and long enough recording (i.e. $\sim 0.4\%$ peak density and 1,000 frames).

Mathematical Appendix 4

Fisher matrix and Cramer-Rao bound (CRB)

Computing the Fisher matrix allows to determine the Cramer-Rao bound for each parameter. Establishing the theoretical lower bound of experimental errors allows in turn a rigorous evaluation of the results accuracy.

Log-likelihood of the observation, as modeled by

$$X_n = I \times G_n(i_0, j_0, r_0) + m + N_n(\sigma^2)$$

H_1 hypothesis: mean background + Gaussian target + Gaussian noise, as already defined (see **Mathematical Appendix 1**).

Fisher information matrix:

$$J(\theta) = E \left[\frac{\partial J}{\partial \theta} \cdot \frac{\partial J}{\partial \theta^t} \right]$$

where $\theta = [m, I, i_0, j_0, r_0, \sigma^2]^t$, vector of all parameters

Any unbiased estimator has an estimation variance limited by

$$\text{var}(\hat{\theta}) \geq \text{CRB} = J^{-1}(\theta), \text{ Cramer-Rao lower bounds}$$

$$J(\theta) = \begin{bmatrix} \frac{w_s^2}{\sigma^2} & \frac{1}{\sigma^2} \sum G & \frac{I}{\sigma^2} \sum \frac{\partial G}{\partial i_0} & \dots \frac{\partial G}{\partial j_0} & \dots \frac{\partial G}{\partial r_0} & 0 \\ & \frac{1}{\sigma^2} & \frac{I}{\sigma^2} \sum G \frac{\partial G}{\partial i_0} & \dots G \frac{\partial G}{\partial j_0} & \dots G \frac{\partial G}{\partial r_0} & 0 \\ & & \frac{I^2}{\sigma^2} \sum \left(\frac{\partial G}{\partial i_0} \right)^2 & \dots \frac{\partial G}{\partial i_0} \frac{\partial G}{\partial j_0} & \dots \frac{\partial G}{\partial i_0} \frac{\partial G}{\partial r_0} & 0 \\ & & & \dots \left(\frac{\partial G}{\partial j_0} \right)^2 & \dots \frac{\partial G}{\partial j_0} \frac{\partial G}{\partial r_0} & 0 \\ & & & & \dots \left(\frac{\partial G}{\partial r_0} \right)^2 & 0 \\ & & & & & \frac{w_s^2}{2\sigma^4} \end{bmatrix}$$

w_s is the size in pixels of the sliding window considered for summing (i.e. $w_s = 7$).

The Fisher matrix is symmetric (by definition) and block-diagonal for the variable σ^2 (noise power). Coefficients corresponding to j_0 and r_0 have been simplified for clarity and should be completed as shown for i_0 . Numerical computation of the inverse matrix $J^{-1}(\theta)$ and its diagonal leads to the CRB.

Optimal treatment of biological data can thus be performed thanks to information theory tools such as ML functions and the Fisher matrix information. Comparable approaches have already been reported for SDT, both for particle estimation and reconnection⁸⁻¹¹ as well as for other microscopy methods, such as FRET¹² (see ref.⁵ for a comprehensive review). The Fisher matrix, and thus the CRB, relies on a given modeling, as defined by equation [1] in the present work. Hence, a method such as the 3-point estimator⁸, using the assumption of detecting a Gaussian peak with Gaussian noise, can be directly compared with MTT (**Fig. 4b**). However, such a direct comparison is no longer possible when the modeling differs, affecting the CRB. The present work has been restricted to particle detection in 2D images. 3D extensions of this problem have been proposed either using cylindrical optics with qdots¹³ or STORM¹⁴, 2-photon microscopy¹⁵, time-lapse z-stacks¹¹ or defocused imaging¹⁰. By computing the CRB, the later demonstrates an optimal sub-resolution axial detection¹⁰.

Supplementary References

1. Osborn, M. and Weber, K., Immunofluorescence and immunocytochemical procedures with affinity purified antibodies: tubulin-containing structures. *Methods Cell Biol.* **24**, 97-132 (1982).
2. Bouchaud, J.P. and Georges, A., Anomalous Diffusion in Disordered Media - Statistical Mechanisms, Models and Physical Applications. *Physics Reports-Review Section of Physics Letters* **195**, 127-293 (1990).

3. Papoulis, A., in *Probability, Random Variables and Stochastic Process* (McGraw Hill, 2001), pp. 277.
4. Van Trees, H.L., *Detection, Estimation, and Modulation Theory*. (Wiley Inter-Science, 1968).
5. Kalaidzidis, Y., Intracellular objects tracking. *Eur. J. Cell Biol.* **86**, 569-578 (2007).
6. Gelles, J., Schnapp, B.J., and Sheetz, M.P., Tracking kinesin-driven movements with nanometre-scale precision. *Nature* **331**, 450-453. (1988).
7. Thompson, R.E., Larson, D.R., and Webb, W.W., Precise nanometer localization analysis for individual fluorescent probes. *Biophys. J.* **82**, 2775-2783 (2002).
8. Bonneau, S., Dahan, M., and Cohen, L.D., Single quantum dot tracking based on perceptual grouping using minimal paths in a spatiotemporal volume. *IEEE Trans. Image Process.* **14**, 1384-1395 (2005).
9. Ober, R.J., Ram, S., and Ward, E.S., Localization accuracy in single-molecule microscopy. *Biophys. J.* **86**, 1185-1200 (2004).
10. Aguet, F., Van De Ville, D., and Unser, M., A maximum-likelihood formalism for sub-resolution axial localization of fluorescent nanoparticles. *Opt. Express* **13**, 10503-10522 (2005).
11. Genovesio, A., Liedl, T., Emiliani, V., Parak, W.J., Coppey-Moisand, M., and Olivo-Marin, J.C., Multiple particle tracking in 3-D+t microscopy: method and application to the tracking of endocytosed quantum dots. *IEEE Trans Image Process* **15**, 1062-1070 (2006).
12. Watkins, L.P. and Yang, H., Information bounds and optimal analysis of dynamic single molecule measurements. *Biophys. J.* **86**, 4015-4029 (2004).
13. Holtzer, L., Meckel, T., and Schmidt, T., Nanometric three-dimensional tracking of individual quantum dots in cells. *Applied Physics Letters* **90**, 053902 (2007).
14. Huang, B., Wang, W., Bates, M., and Zhuang, X., Three-dimensional super-resolution imaging by stochastic optical reconstruction microscopy. *Science* **319**, 810-813 (2008).
15. Ragan, T., Huang, H., So, P., and Gratton, E., 3D particle tracking on a two-photon microscope. *J. Fluoresc.* **16**, 325-336 (2006).